ISSN 1674-1056
http://cpb.iphy.ac.cn
http://iopscience.iop.org/cpb
中国物理 B
Chinese Physics
中国物理
Chinese Physics B

# Gas flow characteristics of argon inductively coupled plasma and advections of plasma species under incompressible and compressible flows

Shu-Xia Zhao(赵书霞), Zhao Feng(丰嚣)

**Citation:**Chin. Phys. B . 2018, 27(12): 124701. **doi:** 10.1088/1674-1056/27/12/124701
Journal homepage: http://cpb.iphy.ac.cn; http://iopscience.iop.org/cpb

**What follows is a list of articles you may be interested in**

---

## Achieving acoustic cloak by using compressible background flow

Ruo-Yang Zhang(张若洋), Qing Zhao(赵清), Mo-Lin Ge(葛墨林)

Chin. Phys. B . 2016, 25(8): 084702. **doi:** 10.1088/1674-1056/25/8/084702

## Dual solutions in boundary layer flow of Maxwell fluid over a porous shrinking sheet

Krishnendu Bhattacharyya, Tasawar Hayat, Ahmed Alsaedi

Chin. Phys. B . 2014, 23(12): 124701. **doi:** 10.1088/1674-1056/23/12/124701

## Bifurcation phenomena and control for magnetohydrodynamic flows in a smooth expanded channel

G. C. Layek, Mani Shankar Mandal, H. A. Khalaf

Chin. Phys. B . 2014, 23(11): 114701. **doi:** 10.1088/1674-1056/23/11/114701

## Longitudinal and transverse structure functions in decaying nearly homogeneous and isotropic turbulence

Imtiaz Ahmad, Lu Zhi-Ming, Liu Yu-Lu

Chin. Phys. B . 2014, 23(1): 014701. **doi:** 10.1088/1674-1056/23/1/014701

## FEM simulations and experimental studies of the temperature field in a large diamond crystal growth cell

Li Zhan-Chang, Jia Xiao-Peng, Huang Guo-Feng, Hu Mei-Hua, Li Yong, Yan Bing-Min, Ma Hong-An

Chin. Phys. B . 2013, 22(1): 014701. **doi:** 10.1088/1674-1056/22/1/014701

---

# Gas flow characteristics of argon inductively coupled plasma and advections of plasma species under incompressible and compressible flows*

Shu-Xia Zhao(赵书霞)† and Zhao Feng(丰曌)

*Physics Department, Dalian University of Technology, Dalian* 116024, *China*

(Received 7 June 2018; revised manuscript received 3 October 2018; published online 10 November 2018)

In this work, incompressible and compressible flows of background gas are characterized in argon inductively coupled plasma by using a fluid model, and the respective influence of the two flows on the plasma properties is specified. In the incompressible flow, only the velocity variable is calculated, while in the compressible flow, both the velocity and density variables are calculated. The compressible flow is more realistic; nevertheless, a comparison of the two types of flow is convenient for people to investigate the respective role of velocity and density variables. The peripheral symmetric profile of metastable density near the chamber sidewall is broken in the incompressible flow. At the compressible flow, the electron density increases and the electron temperature decreases. Meanwhile, the metastable density peak shifts to the dielectric window from the discharge center, besides for the peripheral density profile distortion, similar to the incompressible flow. The velocity profile at incompressible flow is not altered when changing the inlet velocity, whereas clear peak shift of velocity profile from the inlet to the outlet at compressible flow is observed as increasing the gas flow rate. The shift of velocity peak is more obvious at low pressures for it is easy to compress the rarefied gas. The velocity profile variations at compressible flow show people the concrete residing processes of background molecule and plasma species in the chamber at different flow rates. Of more significance is it implied that in the usual linear method that people use to calculate the residence time, one important parameter in the gas flow dynamics, needs to be rectified. The spatial profile of pressure simulated exhibits obvious spatial gradient. This is helpful for experimentalists to understand their gas pressure measurements that are always taken at the chamber outlet. At the end, the work specification and limitations are listed.

**Keywords:** gas flow, inductively coupled plasma, compressible flow, fluid model

**PACS:** 47.10.ad, 47.11.Fg, 47.15.–x, 52.30.Ex **DOI:** 10.1088/1674-1056/27/12/124701

## 1. Introduction

In low-pressure radio frequency plasma sources, the gas flow and heating, together with the neutral depletion, comprise the background gas dynamics. The gas dynamics are tightly coupled to the process of plasma production and transport, via their missions of providing feedstock species, exposing plasma to advection, re-distributing deposited energy, *etc*. Hence, investigations on the gas dynamics are useful for people to understand the plasma properties and processing techniques, in view of their attendance in delivering impinging ions and reactive radicals to the surfaces, where the material etching or film deposition is conducted. At present, most efforts on the gas heating scheme were aimed at measuring the gas temperature[1–3] and analyzing the heating mechanism,[4–6] *e.g.*, elastic and charge exchange collisions and Franck–Condon. In addition, the influence of the gas heating on the magnitudes of electron density and temperature,[7] the varying trend of electron temperature against power,[8] the wave magnetic fields and skin effect,[9] *etc.*, are also specified. As analyzed, the neutral depletion[10–13] is actually caused cooperatively by the pressure balance and gas heating. It could enhance plasma transport and result in non-monotonic variation of plasma density versus power.[14]

The gas flow[15,16] is caused by the system that feeds gas into the reactor and the pumping setup. A gas flow channel is formed between the locations of gas entrance nozzle and pumping port. The gas flow rate and the channel, together with the chamber dimension, cooperatively determine the residence time of feedstock gas in the reactor.[17,18] This parameter is important as it might be comparative to the timescale of plasma species crossing over the reactor via the diffusive and drift process and that of the chemical reactions with metastables. As a result, the plasma species densities changed with the residence time, as observed in Ref. [19]. In addition, the density profile alters when changing the gap between the electrodes due to the competition of the above time scales,[20] or by considering a gas flow module into the fluid model or not,[21] in a capacitively coupled plasma source. Still, the gas flow, together with the feedstock gas fragmentation, multi component mass transport, gas heating, pumping speed, *etc.*, influence the accuracy of gas pressure measurements at the chamber outlet. Lastly, the pressure, spatially averaged, should increase with increasing the gas flow rate, which influence the plasma. In Ref. [22], the electron density and collisional power loss in-

*Project supported by the National Natural Science Foundations of China (Grant No. 11305023). The author is deeply indebted to the Dalian University of Technology for providing the authority of utilizing the COMSOL software.

†Corresponding author. E-mail: zhaonie@dlut.edu.cn

© 2018 Chinese Physical Society and IOP Publishing Ltd 

creased and the electron temperature decreased with the gas flow rate, in an inductively coupled Ar/$N_2$ plasma. All the above studies focus on the influence of gas flow on the plasma properties. Other gas flow works report on its inference on the aspects that relate to the plasma processing techniques, *e.g.*, the ion flux profile,[23] the saturate current densities and its dependence on gas type (Ar versus $C_4F_8$),[24] the ion energy and angular distribution functions,[25] the Si etch rate with $SF_6$ plasma,[26] the uniformity of deposition rate of hydrogenated silicon nitride film,[27] and the life cycle of silicon chloride etch product.[28]

The above literature review tells us that the gas flow plays very important role in both the plasma itself and the related processes. This is contradictory to the assertion that it had minor influence on the plasma due to the dominance of diffusion over advection in the bulk plasma, which was given early in Refs. [29] and [30]. We believe that the gas flow only exhibits its importance under certain conditions, which is cooperatively determined by the coupling mechanism of all the above factors mentioned, such as the residence time, chemical kinetics, pressure measurements, gas heating, feedstock molecules fragmentation, neutral depletion and pumping system, *etc*. Hence, it is of great importance to investigate the gas flow effect systematically. As reviewed, the gas flow effect in inductively coupled plasmas (ICPs) has been studied by several works. However, we feel that these studies are not enough, and not systematic either. For instance, the influence of gas flow on the density profiles of neutral species is yet reported. The magnitudes of diffusive and advective velocities of neutrals are in the same order, at strong flows. Hence, the advection ought to disturb the conventional density profiles of neutrals that are formed via pure diffusion, as expected. Besides, although the basic characteristics of flow velocity, *i.e.*, streamline and magnitude, were given in Refs. [30] and [31], detailed structure, *e.g.*, axial and radial velocity profiles, and their evolution as a function of flow rate and pressure, are not studied yet.

In this work, a two-dimensional fluid model is used to investigate the characteristics of background gas flow in an argon ICP, and meanwhile the advections of plasma species at incompressible and compressible gas flows are discussed. Logically, the compressible flow is more realistic. Nevertheless, we found that the utilization of incompressible flow and of its comparison to the compressible flow, can be very helpful for us to understand the respective behavior of velocity and density variables and their influence on the plasma. The pressures used in this work are selected in a range, *i.e.*, 20 mTorr $\sim$ 50 mTorr (1 Torr $= 1.33322 \times 10^2$ Pa), such that the gas flow kinetics studied are in the domain of fluid model. Meanwhile, at these pressures and the discharge frequency of 13.56 MHz, the experimentally measured electron energy distribution functions are found more or less Maxwellian,[32–35] which meets the requirement of electron fluid equations.

## 2. Model description

### 2.1. Chamber configuration, spatial discretization and reaction set

The two-dimensional axial symmetric ICP reactor used in this model is shown in Fig. 1. In the matching box that is filled with air, a two-turn coil with the thickness of 0.6 cm is placed above the quartz window. The turns of the coil are 6.0 cm and 10.0 cm in radius, respectively. The coil is supplied with a radio frequency power source of 13.56 MHz. In the simulations, the coil current is tuned until the total deposited power in the chamber, defined as spatial integration of the electron power density, equals to the pre-designed value, *i.e.*, 200.0 W. The working gas is delivered into the chamber from the circular open loop around the roof edge of discharging chamber and expelled away via pumping system at the chamber outlet. The total height of the chamber is 17.0 cm. The window and the matching box are both 14.0 cm in radius, and the discharging chamber beneath them is 15.0 cm in radius. The window width is 1.0 cm and the box height is 3.0 cm. A grounded substrate is seated at the bottom of the chamber, with its radius and height fixed at 13.0 cm and 4.0 cm, respectively.

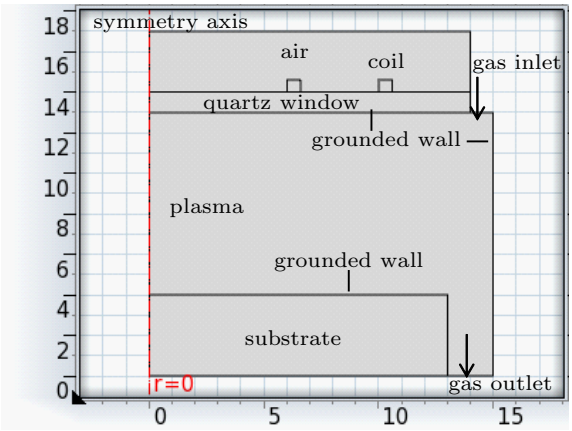



**Fig. 1.** (color online) ICP chamber used in the simulations

The gas phase and surface chemistries of argon plasma used in this model are listed in Tables 1 and 2, respectively. Four types of species are considered, *i.e.*, electrons, argon ions $Ar^+$, metastable argon atoms $Ar_m$, and grounded atoms Ar. In Table 1, the following collision types are included, *i.e.*, elastic, electronic excitation, de-excitation, direct ionization, multistep ionization, Penning ionization and metastable quenching. These different rate coefficients of electron collisions are calculated via the integration of the Maxwellian electron energy distribution function with their respective cross section set. The rate coefficients of all heavy species reactions are given as constants. Upon arriving at chamber surface, the argon ions are neutralized and the metastables are de-excited, and they both return to the ground state, as illustrated in Table 2. The sticking coefficients of ions and metastables at the surfaces both equal to 1.0.

**Table 1.** Gas phase electron impact collisions and chemical reactions.[36]

| Reaction | Formula | Type | $\Delta\varepsilon$/eV | Rate coefficients[a] |
|---|---|---|---|---|
| 1 | $e + Ar \Longrightarrow e + Ar$ | elastic | 0 | $c$ |
| 2 | $e + Ar \Longrightarrow e + Ar_m$ | excitation | 11.5 | $c$ |
| 3 | $e + Ar_m \Longrightarrow e + Ar$ | de-excitation | −11.5 | $c$ |
| 4 | $e + Ar \Longrightarrow 2e + Ar^+$ | direct ionization | 15.8 | $c$ |
| 5 | $e + Ar_m \Longrightarrow 2e + Ar^+$ | multistep ionization | 4.24 | $c$ |
| 6 | $Ar_m + Ar_m \Longrightarrow e + Ar + Ar^+$ | penning ionization | 0 | $3.734 \times 10^8$ |
| 7 | $Ar_m + Ar \Longrightarrow Ar + Ar$ | metastable quenching | 0 | 1807 |

[a]The unit of rate coefficient is $m^3/s{\cdot}mol$.

The space of the ICP chamber is discretized by the finite element method. The mesh set used in the simulations, *i.e.*, mesh set I, is shown in Fig. 2(a). There are totally 17400 mesh elements that fill up the geometry, among which 9559 elements are triangle and 7841 are quadrilateral. Note that the fine mesh is used around the coil to resolve the skin effect of electromagnetic field and the boundary layer meshes are created around the plasma region border to capture the space charge separation between electrons and ions.[37] To discuss numerical errors, the dependence of simulation results on mesh size are tested. We believe that the errors are more related to the mesh size of plasma region; hence the test is carried on the original mesh of Fig. 2(a) and a new mesh set that holds fine mesh in the plasma region, *i.e.*, mesh set II, as shown in Fig. 2(b). The tests show that the absolute relative differences of electron densities and temperatures that are calculated by using mesh sets I and II, respectively, are about 0.05%. The difference is tiny, and the simulation results are hence independent of the mesh size.

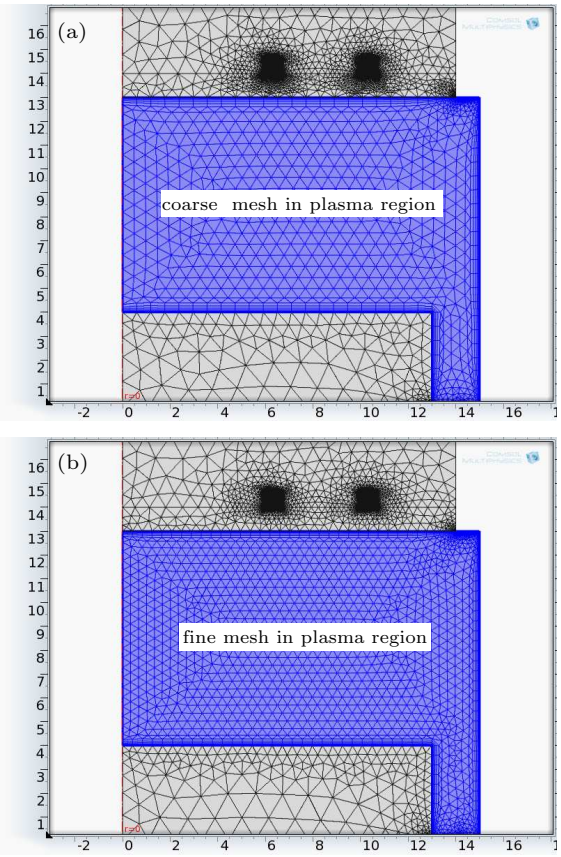



**Fig. 2.** (color online) (a) Mesh set I is used for the spatial discretization of ICP chamber in the simulations. (b) Mesh set II holds fine mesh in the plasma region as compared to mesh set I. It is used to test the dependence of simulation results on mesh size, *i.e.*, numerical errors. The tests show that the absolute relative differences of electron densities and temperatures that are calculated by using mesh sets I and II, respectively, are about 0.05%. The difference is tiny, and the simulation results are hence independent of the mesh size.

**Table 2.** Surface reactions mechanism.

| Reaction | Formula | Sticking coefficient |
|---|---|---|
| 1 | $Ar_m \Longrightarrow Ar$ | 1 |
| 2 | $Ar^+ \Longrightarrow Ar$ | 1 |

### 2.2. Formulation of the model

The inductively coupled plasma (ICP) and the single-phase flow (SPF) modules of the COMSOL software are taken for this gas flow study. The former module describes the plasma generation and transport, while the latter describes the background gas flow. The ICP module consists of electron, heavy species, electromagnetic field, and electrostatic field equations. In the SPF module, the Navier–Stocks equation is selected to study the incompressible gas flow, and the momentum conservation equation is selected for the compressible gas flow. The flow velocity and density of gas mixture, calculated from the SPF module, are sent to the ICP module in the compressible flow, while only the velocity variable is delivered in the incompressible flow. Reversely, the ICP module calculates the viscosity coefficient of gas mixture and transfer it to the two types of gas flow, besides for describing the plasma transport. The interacting mechanism of the two modules is shown in Fig. 3. The equations of each module will be elaborated next.

#### 2.2.1. Electron equations

The equations of electron density and energy are expressed as

$$\begin{aligned} &\frac{\partial n_e}{\partial t} + \nabla \cdot \boldsymbol{\Gamma}_e = R_e - (\boldsymbol{u} \cdot \nabla) n_e, \\ &\frac{\partial n_\varepsilon}{\partial t} + \nabla \cdot \boldsymbol{\Gamma}_\varepsilon + \boldsymbol{E} \cdot \boldsymbol{\Gamma}_e = R_\varepsilon - (\boldsymbol{u} \cdot \nabla) n_\varepsilon + P_{\text{ohm}}. \end{aligned} \quad (1)$$

The drift diffusion approximation is selected for the number and energy flux of electrons, due to the tiny mass of electrons.

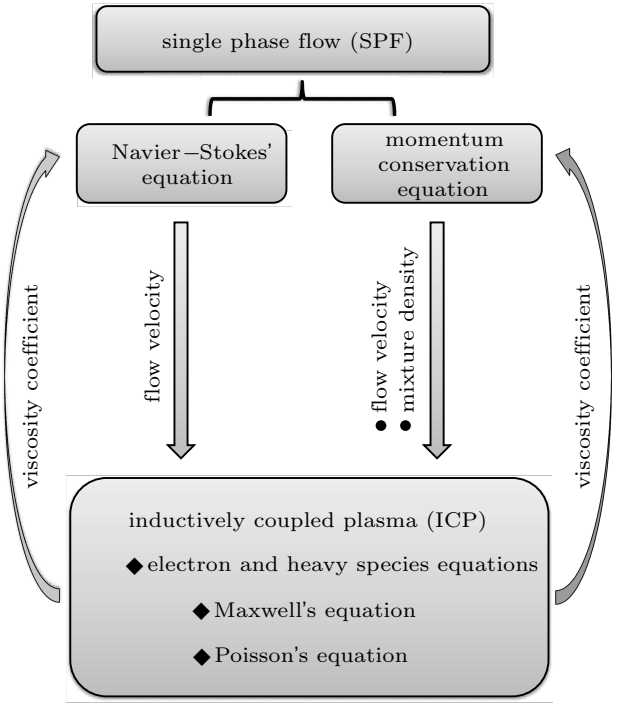



**Fig. 3.** (color online) Interactions of single-phase flow (SPF) and inductively coupled plasma (ICP) modules in this study.

The fluxes of electrons density and energy are described as follows

$$\begin{aligned}\boldsymbol{\Gamma}_{\rm e} &= -(\boldsymbol{\mu}_{\rm e}\cdot\boldsymbol{E})n_{\rm e} - \boldsymbol{D}_{\rm e}\cdot\nabla n_{\rm e},\\ \boldsymbol{\Gamma}_{\varepsilon} &= -(\boldsymbol{\mu}_{\varepsilon}\cdot\boldsymbol{E})n_{\varepsilon} - \boldsymbol{D}_{\varepsilon}\cdot\nabla n_{\varepsilon}.\end{aligned} \tag{2}$$

Here, $n_{\rm e}$ and $n_{\varepsilon}$ are the number and energy densities of electrons. $\boldsymbol{\mu}_{\rm e}$ and $\boldsymbol{\mu}_{\varepsilon}$ are the number and energy mobility coefficients. $\boldsymbol{D}_{\rm e}$ and $\boldsymbol{D}_{\varepsilon}$ are the number and energy diffusivity coefficients. These above coefficients are related with each other, via the formulas, $\boldsymbol{D}_{\rm e} = \boldsymbol{\mu}_{\rm e}T_{\rm e}$, $\boldsymbol{D}_{\varepsilon} = \boldsymbol{\mu}_{\varepsilon}T_{\rm e}$, and $\boldsymbol{\mu}_{\varepsilon} = (5/3)\boldsymbol{\mu}_{\rm e}$. $R_{\rm e}$ and $R_{\varepsilon}$ in Eq. (1) are source terms of the continuity and energy conservation equation, respectively, and they are expressed as

$$\begin{aligned}R_{\rm e} &= \sum_{\rm j=1}^{M} l_j k_j \prod_{m=1}^{P} n_m^{\nu_{jm}},\\ R_{\varepsilon} &= \sum_{\rm j=1}^{M} \varepsilon_j l_j k_j \prod_{m=1}^{P} n_m^{\nu_{jm}}.\end{aligned} \tag{3}$$

Here, $l_j$ is the number of electrons created or lost per collision of reactions that generate/deplete electrons. $M$ is the number of such reactions. $k_j$ is the rate coefficient of reaction $j$, taken from Table 1. $n_m$ is the number density of reactant $m$ of reaction $j$. $\nu$ is the stoichiometric coefficient of the reaction, and $P$ is the number of reactants. $\varepsilon_j$ is the energy loss of related electron-impact reaction. The terms of Eq. (1), $(\boldsymbol{u}\cdot\Delta)n_{\rm e}$ and $(\boldsymbol{u}\cdot\Delta)n_{\varepsilon}$, describe the transport of electron mass and energy via the background gas advection, and the gas flow velocity $\boldsymbol{u}$ is calculated from the SPF module. Usually, the electron directional velocity of drift and diffusion is rather higher than advective velocity caused by the gas flow; hence the influence of incompressible advection on the electron is expected to be insignificant. Nevertheless, it will be significantly affected by the mixture density in the compressible gas flow, as revealed later. $P_{\rm ohm}$ is power density deposited into the plasma through the Ohm's heating mechanism,

$$P_{\rm ohm} = \frac{1}{2}{\rm Re}(\sigma|E_{\theta}|^2), \tag{4}$$

where $\sigma$ is the electron conductivity and $E_{\theta}$ is the azimuthal electric field of electromagnetic effect.

Without the secondary electron emissions, the boundary conditions of the continuity and energy equations of electrons are defined as

$$\begin{aligned}\boldsymbol{n}\cdot\boldsymbol{\Gamma}_{\rm e} &= \frac{1-r_{\rm e}}{1+r}\left(\frac{1}{2}\nu_{\rm e,th}n_{\rm e}\right),\\ \boldsymbol{n}\cdot\boldsymbol{\Gamma}_{\varepsilon} &= \frac{1-r_{\rm e}}{1+r_{\rm e}}\left(\frac{5}{6}\nu_{\rm e,th}n_{\rm e}\right),\end{aligned} \tag{5}$$

where $\nu_{\rm e,th}$ is the thermal velocity of electrons and $r_{\rm e}$ is the reflection coefficient of electrons from the chamber surface, which is set to 0.2 in this model.

### 2.2.2. Heavy species equations

The heavy species means all plasma species except the electrons, *i.e.*, grounded and excited argon atoms, and argon ions. In this heavy species module, an approximation is used. If there are totally $Q$ heavy species, only the transports of $Q-1$ species are described directly via the transport equation, *i.e.*,

$$\rho\frac{\partial w_k}{\partial t} + \rho(\boldsymbol{u}\cdot\nabla)w_k = \nabla\cdot\boldsymbol{j}k + R_k. \tag{6}$$

The transport of the $Q^{\rm th}$ heavy species, fixed as the feedstock molecule, is controlled via the mass conversation law, *i.e.*,

$$\rho w_Q = \rho\left(1 - \sum_{k=1}^{Q-1} w_k\right). \tag{7}$$

Here, $\rho$ is the total mass density of heavy species, also named as the mixture density. The contribution of electrons to the gas mixture density is omitted due to its tiny mass weight, as compared to the heavy species. This mixture density is calculated from the SPF module. As known, it is unchangeable in the incompressible flow. Nevertheless, in the compressible flow, it can be both spatially and temporally altered via the compressibility. $w_k$ is the mass fraction of species $k$, and $\boldsymbol{u}$ is the velocity of background gas flow. $\boldsymbol{j}_k$ is the diffusive and drift flux of species $k$ and expressed as

$$\begin{aligned}\boldsymbol{j}_k &= \rho w_k \boldsymbol{V}_k,\\ \boldsymbol{V}_k &= D_{k,m}\nabla\ln(w_k) - z_k\mu_m\boldsymbol{E},\end{aligned} \tag{8}$$

where $\boldsymbol{V}_k$ is the diffusive and drift velocity of species $k$, $z_k$ is elementary charge number of charged species $k$, and $\boldsymbol{E}$ is the electrostatic field of spatial charge density. The multi-component mass diffusion mechanism[38] is taken into account

in this model. $D_{k,m}$ is the diffusion coefficient of the gas mixture and expressed as

$$D_{k,m} = \frac{1-w_k}{\sum\limits_{j\neq k}^{Q} x_j/D_{kj}}, \tag{9}$$

where $x_j$ is the molar fraction of species $j$ and $D_{k,j}$ is binary diffusion coefficient of the Chapman–Enskog theory. $\mu_m$ is the mobility of ions, given by the Einstein's relation. In the Einstein's relation, the ion temperature is assumed room temperature. The validity of this assumption will be discussed in the section of conclusion and further remarks. The source term of heavy species transport equation is expressed as

$$R_k = M_k \sum_{j=1}^{N} l_{k,j} r_j, \tag{10}$$

where $M_k$ is molecular weight, $r_j$ is the rate of reaction $j$ that creates/consumes species $k$, $N$ is the reaction number, and $l_{k,j}$ is the particle number of species $k$ created or lost per collision of reaction $j$. The reaction rate, $r_j$, is expressed as

$$r_j = k_j \prod_{m=1}^{S} c_m^{\nu_{jm}}. \tag{11}$$

In this formula, $k$ is the rate coefficient, $S$ is the number of reactants, $\nu$ is the stoichiometric coefficients, and $c$ is the molar concentration of reactants. The boundary condition of heavy species equation considers the components of the Bohm's velocity, species surface kinetics and advection of gas flow.

### 2.2.3. Electromagnetic equations

The electromagnetic field in this discharge is calculated via the following equation,

$$\left(\mathrm{j}\omega\sigma - \omega^2\varepsilon_0\varepsilon_\mathrm{r}\right)\boldsymbol{A} + \nabla\times\left(\mu_0^{-1}\mu_\mathrm{r}^{-1}\boldsymbol{B}\right) = \boldsymbol{J}_\mathrm{a}, \tag{12}$$

which is deduced from the Maxwell's equation (details about this deduction can be found in the appendix). Here, j is the imaginary unit and $\omega$ is the angular frequency, $\varepsilon_0$ and $\varepsilon_\mathrm{r}$ are the vacuum permittivity and the relative permittivity of specific media, $\mu_0$ and $\mu_\mathrm{r}$ are the vacuum permeability and the relative permeability of specific media, $\boldsymbol{A}$ is the magnetic vector potential and $\boldsymbol{J}_\mathrm{a}$ is the applied coil current. $\sigma$ is the electron conductivity and calculated as,

$$\sigma = \frac{n_\mathrm{e}q^2}{m_\mathrm{e}(\nu_\mathrm{e}+\mathrm{j}\varpi)}, \tag{13}$$

where $n_\mathrm{e}$ is the electron number density; $m_\mathrm{e}$ and $q$ are the electron mass and charge, respectively; and $\nu_\mathrm{e}$ is the collision frequency of electrons with neutrals. The magnetic insulation condition, $\boldsymbol{n}\times\boldsymbol{A} = 0$, is taken as boundary for this electromagnetic equation. Note that the general inductive discharges operate at two modes, *i.e.*, E and H modes. In our present study, only the H mode is discussed. The above electromagnetic vector equation presented actually can describe both the E and H mode discharges. We therefore in the appendix illustrate explicitly how to use this equation to describe the H mode discharge.

### 2.2.4. Electrostatic equations

The Poisson's equation is used to calculate the electrostatic field,

$$\boldsymbol{E} = -\nabla V,\ \ \nabla\cdot\boldsymbol{D} = \rho_V, \tag{14}$$

where $\rho_V$ is the charge density of the space. The boundary condition of zero potential is used at chamber surfaces that are grounded, such as the sidewall and the bottom, while the condition of surface charge accumulation, *i.e.*,

$$\frac{\partial\rho_\mathrm{s}}{\partial t} = \boldsymbol{n}\cdot\boldsymbol{J}_i + \boldsymbol{n}\cdot\boldsymbol{J}_\mathrm{e},\ \ -\boldsymbol{n}\cdot\boldsymbol{D} = \rho_\mathrm{s} \tag{15}$$

is used at the surface of dielectric window. Here, $\rho_\mathrm{s}$ is the surface charge density, accumulated by the fluxes of arriving ion and electron. $\boldsymbol{n}$ is the normal unit vector of dielectric window surface. $\boldsymbol{D}$ is the electric displacement vector and related to the electrostatic field via the formula, $\boldsymbol{D} = \varepsilon_\mathrm{r}\varepsilon_0\boldsymbol{E}$.

### 2.2.5. The Navier–Stocks equation for gas flow

When the temperature variation in the gas flow is insignificant and the flow velocity is low, *i.e.*, with the Mach number less than 0.3, the flow can be assumed incompressible.[39] The Navier–Stocks equation can therefore be used, *i.e.*,

$$\rho\nabla\cdot\boldsymbol{u} = 0,\ \ \rho(\boldsymbol{u}\cdot\nabla)\boldsymbol{u} = \nabla\cdot\left[-p\boldsymbol{I} + \mu\left(\nabla\boldsymbol{u} + (\nabla\boldsymbol{u})^\mathrm{T}\right)\right]. \tag{16}$$

Here $\mu$ is the gas dynamic viscosity and $\boldsymbol{u}$ is the mass weighted flow velocity. In the incompressible flow, the pressure, $p$, has actually no physical meaning, while the pressure gradient formed is useful for it drives the gas flow. $\rho$ is the total mass density of gas mixture and unaltered in the incompressible flow.

Slip velocity at the walls is negligible in this work due to the selected high-pressure range and no-slip boundary condition is therefore used. At the gas inlet, fixed inlet velocities are taken as boundary condition. At the chamber outlet, fixed gas pressure boundary condition is used. In the incompressible flow, the gas mixture density is fixed in the whole space, whose value is given via the state equation of ideal gas with the outlet pressure and the room gas temperature. Here, the validity of assuming room gas temperature will be discussed in the section of discussion and further remarks.

### 2.2.6. Momentum conservation equation of gas flow

When the compressibility is taken into account, the continuity and momentum conservation equations are used for the gas flow, *i.e.*,

$$\nabla\cdot(\rho\boldsymbol{u}) = 0,$$
$$\rho(\boldsymbol{u}\cdot\nabla)\boldsymbol{u} = \nabla\cdot\left[-p\boldsymbol{I} + \mu\left(\nabla\boldsymbol{u} + (\nabla\boldsymbol{u})^\mathrm{T}\right)\right.$$

$$-\frac{2}{3}\mu(\nabla\cdot\boldsymbol{u})\boldsymbol{I}\Big]+\boldsymbol{F}. \tag{17}$$

No-slip velocity boundary condition is used at the walls and fixed pressure boundary condition is used at the outlet. At the inlet, the boundary condition of gas flow rate, in a unit of sccm, is taken. In the compressible flow, the pressure itself is meaningful and related to the gas mixture density via the state equation of ideal gas, again at the condition of room gas temperature.

## 3. Results and discussion

### 3.1. Species advection at incompressible flow

In Fig. 4, the velocity profiles of incompressible flow are plotted at the inlet velocity of 200 m/s, the power of 200 W, and the pressure of 20 mTorr. Two peaks occur in the radial velocity profile, which are located under the inlet nozzle and at the substrate corner, respectively. The axial velocities are maximal under the inlet nozzle and second largest in the annular passage between the substrate and the sidewall. As the inlet velocity is axial oriented, the axial velocity magnitude is about one factor larger than the radial velocity. In Fig. 5, the advective mass flux profiles of metastables at the same discharge condition are plotted. Two maxima occur in the radial advective flux, which is similar to the radial velocity. Nevertheless, a tilted "bulb" shape is seen from the axial advective flux profile that is quite different with the morphology of axial velocity. The radial fluxes above the substrate edge are distributed similar to the radial velocity the most. In a small area just beneath the nozzle, where the radial and axial velocities are both peaked, the two components of advective flux, nevertheless, are both minimal. This is because the metastables densities at the locations where the velocities of the two components peak, are quite low. Instead, a blue peak of radial flux and the head of an axial flux bulb occur more in the bulk chamber due to the high metastables densities therein. Of interest is in the outlet passage, where the metastables densities are supposed to be low, prominent axial fluxes are observed. This is related to the novel metastables density profile formed by the gas flow process.

In Fig. 6, the metastables density profiles, when the gas flow, *i.e.*, advection, is not included and at the inlet velocity of 200 m/s, are plotted at the discharge condition of 20 mTorr

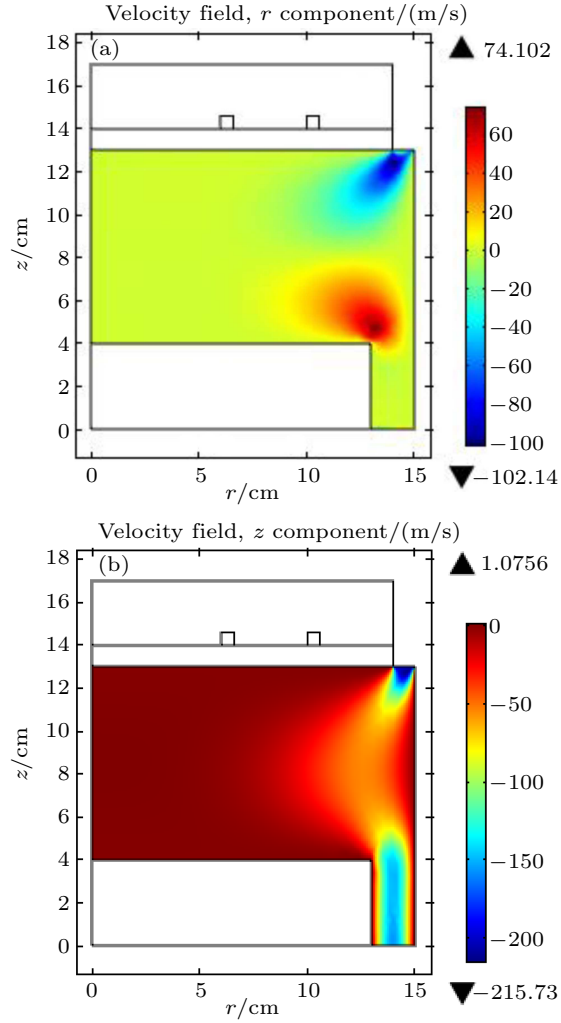



**Fig. 4.** (color online) Profiles of radial (a) and axial (b) velocity components for the inlet velocity of 200 m/s, the power of 200 W and the pressure of 20 mTorr, at the incompressible gas flow.

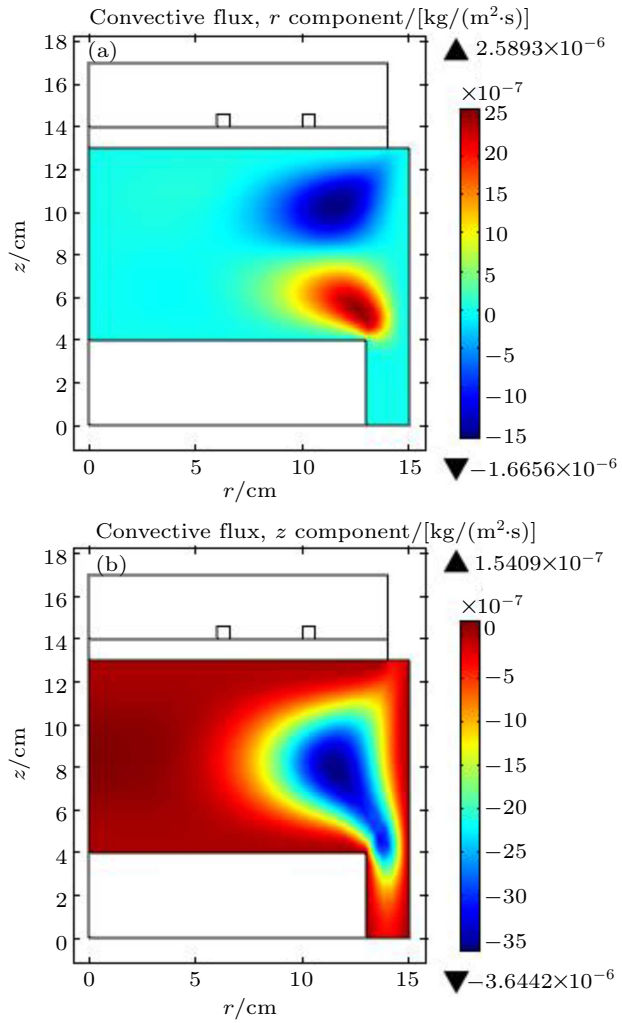



**Fig. 5.** (color online) Profiles of radial (a) and axial (b) advective fluxes of metastables for the inlet velocity of 200 m/s, the power of 200 W and the pressure of 20 mTorr, at the incompressible gas flow.

and 200 W. The density profile without the advection is symmetric with respect to the half height plane of the chamber. At the 200 m/s inlet velocity, this symmetry is destroyed by the advection. In particular, the density profile in the upstream chamber is horizontally compressed inward for the radial diffusion in this region is counteracted by the advective component. In the downstream, the profile is horizontally prolonged outward, which, we believe, is a synergistic effect of radial and axial advective fluxes. The densities of metastables, as well as its axial advective fluxes, near the outlet passage are increased, along with the prolonged density profile in the downstream. The density profile border is in total shifted away from the chamber wall. As a result, the atoms loss on the wall is reduced and the metastables density magnitude is slightly increased.

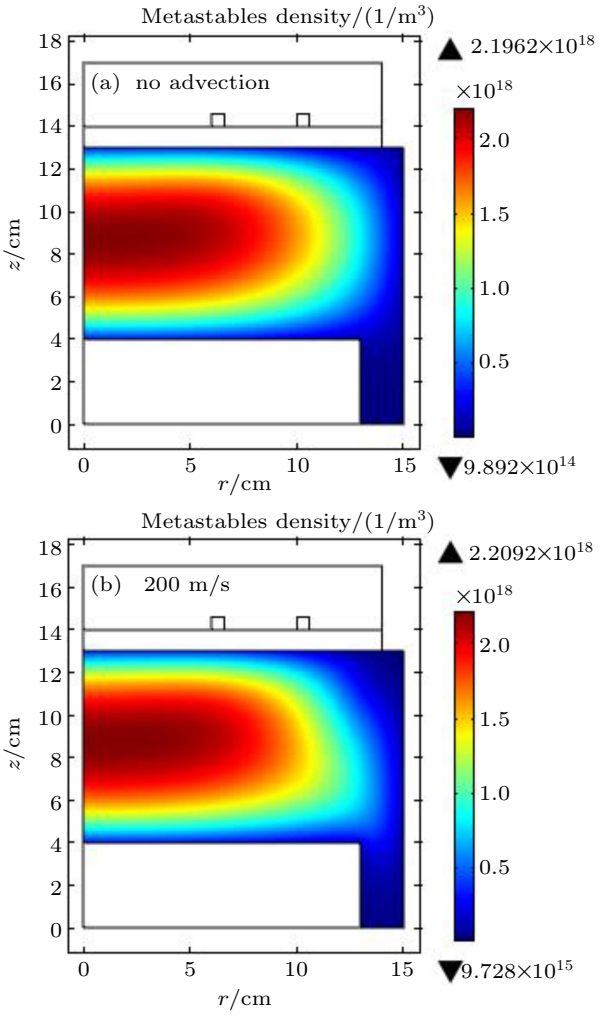



**Fig. 6.** (color online) Metastables density profiles when the gas flow is not included (a) and at 200 m/s inlet velocity, at the discharge condition of 20 mTorr and 200 W.

In Fig. 7, the metastables density profiles when the gas flow is not included and at the inlet velocity of 200 m/s are plotted at the discharge condition of 50 mTorr and 200 W. The metastables density is peaked under the dielectric window, different with the 20 mTorr, because the multistep and Penning ionizations that consume metastables happen more frequently at this pressure. At high pressure, the deformations of density profile, *i.e.*, upstream compression and downstream prolong, via the advection are more obvious. The strong influence of advection on metastables is because the peak of its density profile is close to the gas flow path and the interaction of diffusion and advection is stronger. Moreover, prominent high metastables densities are seen in the passage, as illustrated by a red dashed line circle, formed by strong axial advective fluxes therein. As noted, these high metastables densities of passage could cause diffusions to both the substrate and the sidewall, forming novel double-way diffusion scheme.

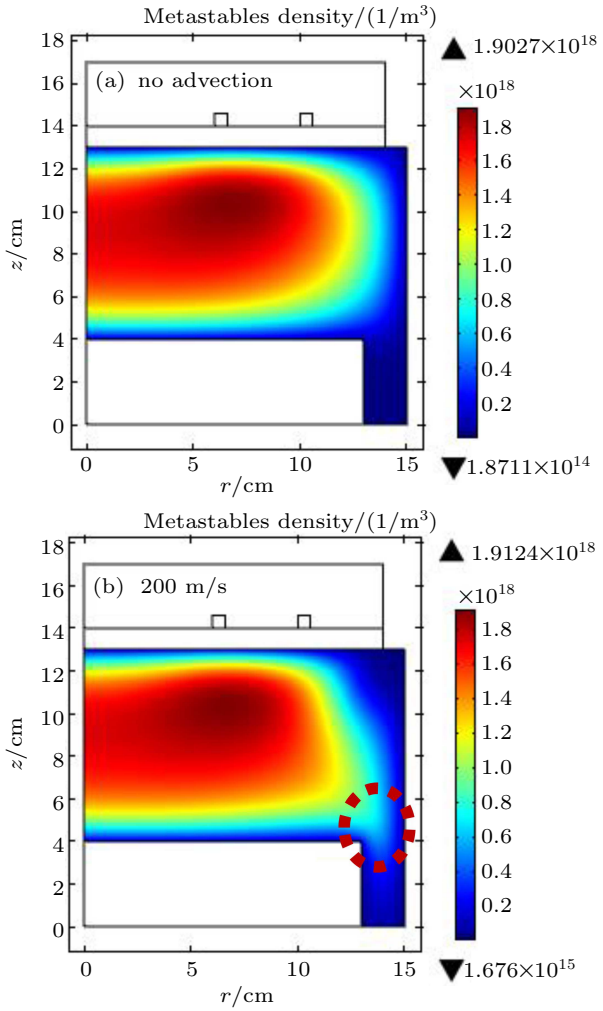



**Fig. 7.** (color online) Metastable density profiles when the gas flow is not included (a) and at 200 m/s inlet velocity, at the discharge condition of 50 mTorr and 200 W.

### 3.2. Species advection under compressible flow

In Figs. 8(a) and 8(b), the metastable density profiles without advection and at the inlet flow rate of 2000 sccm in the scope of compressible flow are plotted, at the discharge condition of 20 mTorr and 200 W. The density profile without advection is symmetric and center peaked. At 2000-sccm flow rate, all distortions of neutral density profile occurred in the incompressible gas flow, *i.e.*, inward shift of upstream

border, outward extension of downstream border, and novel double-way diffusion in the outlet passage, are observed in the compressible flow as well. Besides, the metastable density profile becomes localized and the density magnitude decreases obviously. To explain this new change, in Fig. 8(c) the metastable density profile without advection while at the high pressure of 40 mTorr is plotted, still at the power of 200 W. It is seen that except for the peripheral density profile distortions, the bulk density profile and the peak magnitude of metastables at 40 mTorr when excluding advection are similar to the case of 2000 sccm. It implies that the compressible gas flow seemingly has the same effect as the pressure. To assess this guess, we plot the electronic excitation rate profiles of the above three cases in Fig. 9. It is seen that the peripheral excitation rate profile shifts toward the dielectric window and the peak magnitude of excitation rate increases whenever increasing the flow rate or the pressure, as compared to the 20 mTorr without advection. The electronic excitations are known to occur at high threshold, 11.56 eV and the electron temperature decreases with the pressure due to in-elastic electron collisions. These two effects cooperatively result in the shift of its rate profile toward the coil.

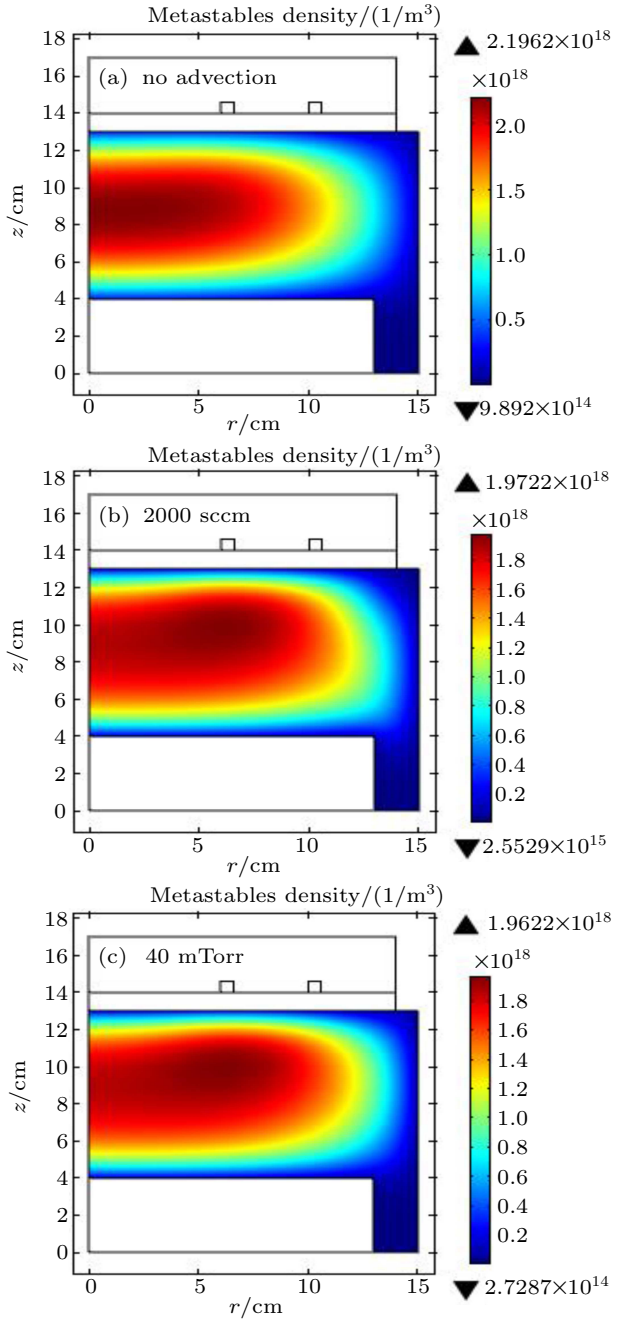



**Fig. 8.** (color online) Metastable density profiles without advection (a) and at 2000 sccm inlet flow rate (b), at the discharge condition of 20 mTorr and 200 W. Also plotted is the metastable density profile of 40 mTorr and 200 W without advection (c) for comparing its profile with the metastable density profile of 2000 sccm (b).

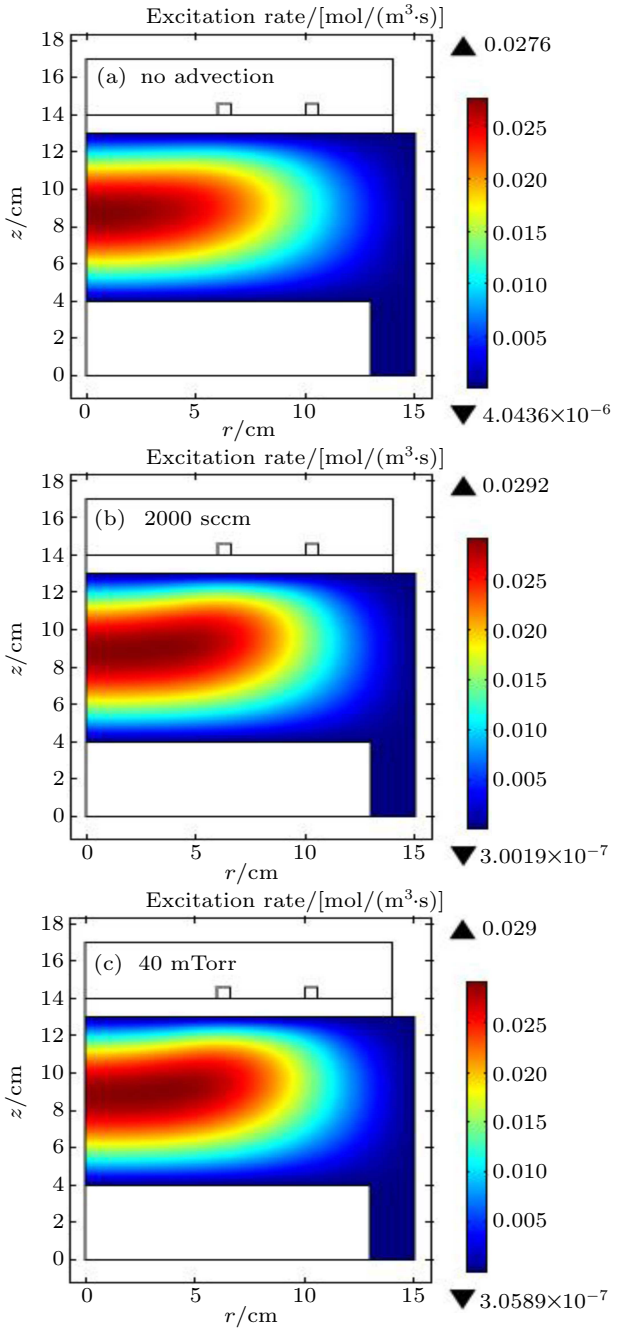



**Fig. 9.** (color online) Electronic excitation rates without advection (a) and at 2000 sccm inlet flow rate (b), at the discharge condition of 20 mTorr and 200 W. Also plotted is the excitation rate at 40 mTorr and 200 W without advection (c) for comparing its profile with the excitation profile of 2000 sccm (b).

In Fig. 10, the peaked values of both electron density and temperature profiles versus the flow rate are plotted, at the discharge condition of 20 mTorr and 200 W. The electron density linearly increases while the temperature monotonically deceases with the flow rate. These trends of electron density and temperature against the flow rate are quite similar to their variations with the pressure,[40] which again testifies that the compressible gas flow and the pressure have the same effects on the plasma, except for the neutral density profile distortions caused by incompressible gas flow. Besides, the variations of electron density and temperature with flow rate, this model predicted, qualitatively agree well with the experimental work of Doh and Horiike,[24] where the electron density decreased and electron temperature increased with the residence time in argon inductive coupled plasma. Here, we believe that the inverse relation between the residence time and the gas flow rate still works.

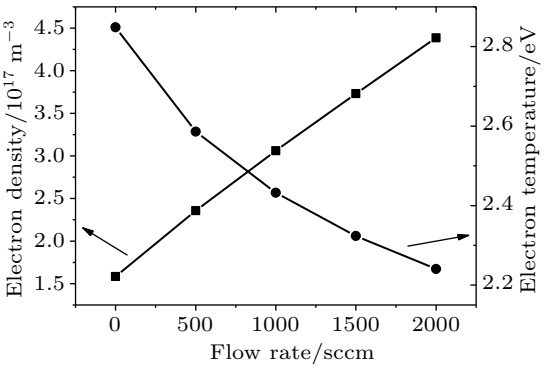



**Fig. 10.** (color online) Peaked values of electron density and temperature profiles versus the gas flow rate at 20 mTorr and 200 W.

To explain the above discovering, in Fig. 11 the calculated gas mixture density profiles of 2000 sccm, with widely and finely resolved legends, respectively, are plotted, at the discharge condition of 20 mTorr and 200 W. At the wide and complete legend resolution, *i.e.*, in Fig. 11(a), the mixture density peaks at the inlet nozzle and sinks at the pumping port. The mixture density minimum at the port, $4.276 \times 10^{-5}$ kg/m$^3$, is calculated via the outlet pressure value, *i.e.*, 20 mTorr, which serves as the boundary condition of the flow equation, based on the state relation of ideal gas. As seen, the most prominent variations of gas mixture density occur at the inlet nozzle and outlet port while it is more or less unchanged in the chamber bulk. At the fine but incomplete color legend resolution, *i.e.*, in Fig. 11(b), the mixture density of bulk chamber lies in a small range of 8.32 kg/m$^3$ $\sim 8.4 \times 10^{-5}$ kg/m$^3$. The three yellow circles in this figure enclose the mixture densities that that are out of the limits of the fine resolution legend. In the experiments, the pressure is always measured at the locations near the outlet port.[40] The simulations reveal that this measurement can severely underestimate the bulk pressure when the pressure is measured at the locations near the outlet. This observation is qualitatively agreeable well with the work of Ref. [41], where the neutral argon density profile was determined in a helicon source by using the spectroscopic measurements and the collisional-radiative model, and the meaning of the measured neutral profile on the ionization degree of bulk plasma was discussed.

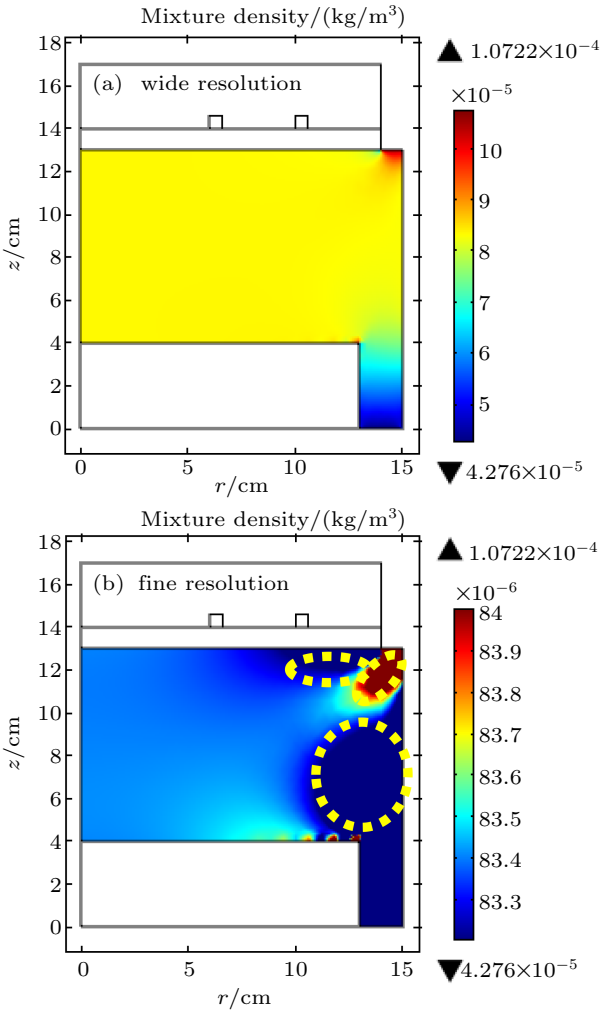



**Fig. 11.** (color online) Calculated gas mixture density profiles with wide (a) and fine (b) resolution legends, at the discharge condition of 20 mTorr, 200 W, and 2000 sccm. In Fig. 11(b), a special way of demonstrating this fine data structure around the chamber periphery is used, *i.e.*, a small range of data, $8.32 \times 10^{-5} \sim 8.4 \times 10^{-5}$, is used to define the color bar while a wide range of actual data, $4.3 \times 10^{-5} \sim 8.4 \times 10^{-5}$, is represented by this color bar.

In Fig. 12(a), the center mixture density versus the flow rate is plotted, at the discharge condition of 20 mTorr and 200 W, together with the outlet mixture density given by the pre-set outlet pressure of 20 mTorr, $4.276 \times 10^{-5}$ kg/m$^3$, that is unvaried with flow. In Fig. 12(b), the mixture density versus pressure without gas flow is plotted. The center mixture density significantly increases with the flow rate, as shown in Fig. 12(a). It resembles the trend of mixture density with pressure in Fig. 12(b). This figure interprets why the compressible flow has the same effect on plasmas as the pressure, *i.e.*, it ac-

tually increases bulk pressure. Note that the present study is based on the boundary condition that fixes pressure at the outlet position, which is frequently used in relevant studies.[22,23] In the real industry or academia lab, the complicated pumping system is installed and the outlet boundary condition is therefore more complex than the fixed pressure. Application of this new outlet boundary condition, *i.e.*, pumping speed and configuration, into the gas flow model should amend the above conclusions to some extent. This is certainly a new interesting work for future.

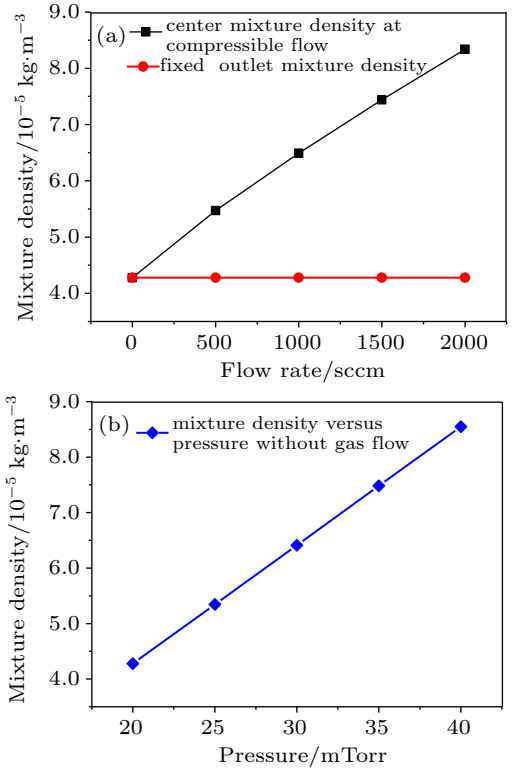



**Fig. 12.** (color online) (a) Center mixture density versus the flow rate and the outlet mixture density that is determined by the outlet pressure of 20 mTorr and unvaried with flow rate, at 20 mTorr and 200 W. The mixture density versus pressure without gas flow at the power of 200 W is plotted(b).

### 3.3. Velocity characteristics of two flows

The velocity magnitude profiles at the inlet velocity of 100 m/s and at the inlet flow rates of 200 sccm and 2000 sccm are sequentially plotted in Fig. 13, at 20 mTorr and 200 W. When the flow is incompressible, and the inlet velocity is 100 m/s, the velocity magnitude peaks at the inlet and the peaked value is 112.8 m/s. The model predicts that the velocity magnitude profile is not changed, but the peaked value linearly increases on increasing the inlet velocity (see Fig. 14(b)). When the flow is compressible and the inlet flow rates are low, *e.g.*, at 200 sccm, the velocity magnitude profile (with a small peaked value of 17.6 m/s) in Fig. 13(b) is similar to that of the incompressible flow. When increasing the flow rate, *e.g.*, to 2000 sccm, the velocity magnitude profile is changed, with its peak shifting from the inlet to the pump port, as shown in Fig. 13(c). This trend is more clear in Fig. 14(a), where the velocity magnitude of pump port increases faster with flow rate than at the inlet.

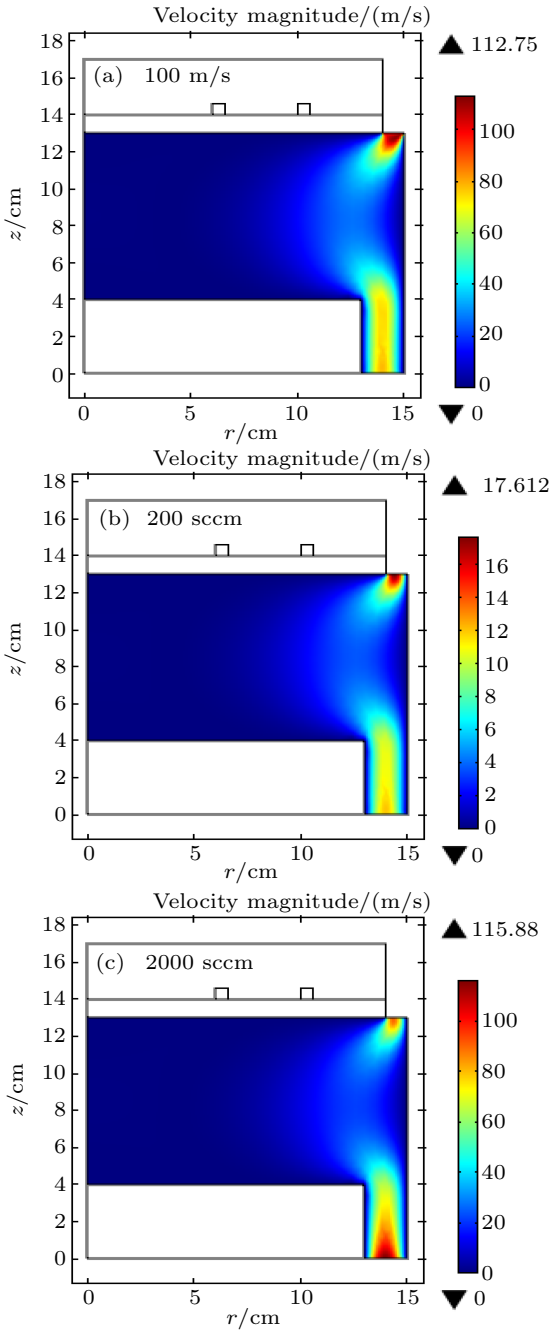



**Fig. 13.** (color online) Velocity magnitude profiles at 100 m/s inlet velocity and incompressible flow (a), and at 200 sccm (b) and 2000 sccm (c) inlet flow rates and compressible flow, at 20 mTorr and 200 W.

The different characteristics of velocity magnitude profiles at the two flows are analyzed. At the incompressible flow with fixed mixture density, the gas flows freely across the chamber. Nevertheless, in the compressible flow the mixture density is varied, and the fluid becomes elastic. It can efficiently respond to the external disturbance via its pressure alteration, proportional to the mixture density alteration, as shown in Fig. 11. At the inlet, the direction of mixture density gradient is along the velocity direction, *i.e.*, from zero to

the maxima. So, the fluid elasticity resists the flow, and the velocity magnitude is reduced. At the pump port, the direction of mixture density gradient is against the velocity direction, from the minimum to zero. So, the fluid elasticity accelerates the flow, and the velocity magnitude is increased. This mechanism can be described by the definition of compressibility, $\nabla \cdot \boldsymbol{u} = -\nabla \ln \rho \cdot \boldsymbol{u}$, analogous to the Poisson's equation that describes the variation of active field with the source term. As seen, at the inlet, an equivalent negative source is formed for the velocity field, while at the port an equivalent positive source term is formed. In addition, at 2000 sccm, obvious gradient of axial velocity is observed in the pumping port channel and meanwhile a maxima of velocity magnitude is formed at the port outlet, as compared to the case of 200 sccm. This is because the gradient of mixture density in the channel holds the same direction as that of the port outlet, both increasing the velocity field; but the increasing rate at the port outlet is stronger, due to the strong mixture density there. Accordingly, the mixture density gradient in the channel at 2000 sccm is stronger than the 200 sccm, as the model predicted. This is a positive feedback process, as the above compressibility equation predicted.

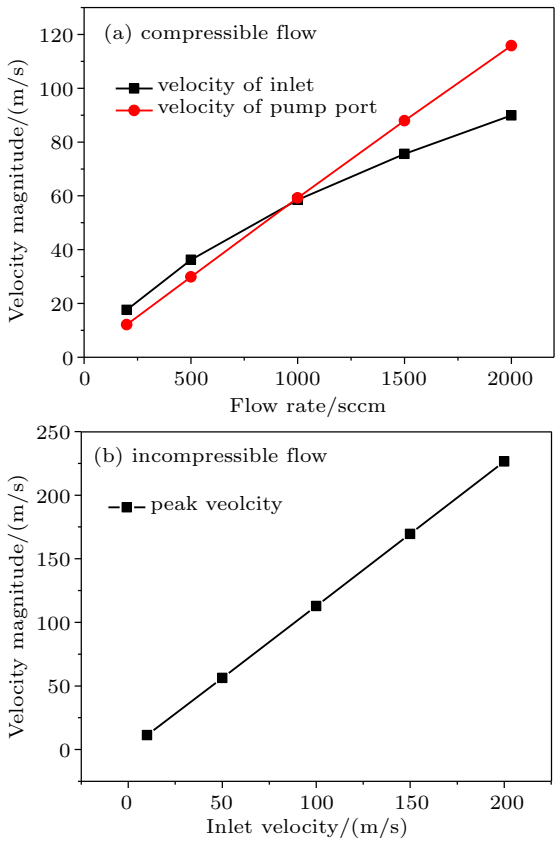



**Fig. 14.** (color online) (a) Velocity magnitudes at the inlet and the pump port of the chamber versus the flow rate at compressible flow and (b) velocity magnitude that is peaked under the inlet nozzle in the profile versus the inlet velocity at incompressible flow, at 20 mTorr and 200 W.

The influence of the compressibility on velocity magnitude profile becomes less important at high pressure, like 50 mTorr in Fig. 15 where the velocity magnitudes at the inlet and pump port both significantly increase with the flow rate. This is because it is more difficult to compress dense gases. As checked, the maximal pressure variation caused by the inlet flow rate of 2000 sccm at 20 mTorr is indeed larger than that of 50 mTorr, *i.e.*, 4.0 Pa versus 3.5 Pa. In addition, the velocity magnitudes at 50 mTorr is totally decreased, as compared with the 20 mTorr, due to the high viscosity at high pressures.

The flow velocity profile is tightly related with the residence time calculations and depicts the picture of plasma species residing in the chamber. Moreover, the velocity magnitude profile evolution implies that the residence time of background gas in the chamber might not be proportional to the gas flow rate, which is contradictory to the present recognition that based on one simple formula, $\tau_{\mathrm{r}} = pV/(p_{\mathrm{atm}}Q)$, where $p$ is the gas pressure, $V$ is the plasma volume, $Q$ is the gas flow rate in units of standard cubic centimeter per minute (sccm), and $Q_{\mathrm{atm}}$ is defined as atmosphere pressure.[42] The literature review revealed the importance of residence time in both the plasma dynamics and etching and deposition process.

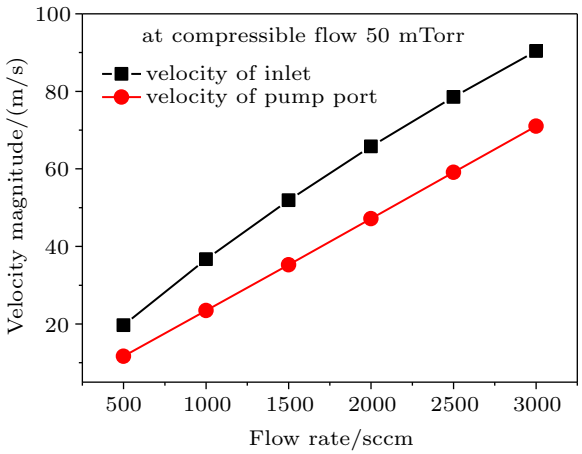



**Fig. 15.** (color online) Velocity magnitudes at the inlet and the pump port of the chamber versus the flow rate at compressible flow and 50 mTorr and 200 W.

## 4. Conclusion and further remarks

In this work, the characteristics of both incompressible and compressible background gas flows and their influences on plasma in argon inductively coupled plasmas are investigated by a fluid model. The results show that incompressible flow can distort the conventional symmetric metastable density profile, and the compressible advection can bring to pressure effect, besides the neutral density profile distortions. The velocity profile of incompressible flow does not change as increasing the inlet velocity, while the velocity peak of compressible flow shifts from inlet to the pump port on increasing flow rate, due to the compressibility. The compressibility influence on velocity magnitude profile become less important at high pressure because of the difficulties in compressing dense gases. The compressible mixture density is considerably varied in gas flow channel, while more or less unchangeable in

bulk chamber. This work helps people understand the relation of measured discharge pressure with the real bulk chamber pressure. Meanwhile, it reveals novel neutral density profiles via incompressible flow and depicts the resident process of plasma species via the flow velocity profile.

As described in the literature, the plasma transport can be substantially influenced by the neutral depletion process that is caused by gas heating effect and pressure balance.[10–14] This attendance of gas temperature in plasma dynamics is important only at rather high deposited power values, *i.e.*, several kilowatts,[13,14] when the feedstock gas is severally depleted, plasma density is high enough, *i.e.*, above $10^{18}$ cm$^{-3}$, and the ionizing degree is high enough, *i.e.*, larger than one percent. This is because that the gas heating effect is more obvious at high powers due to high plasma density and hence high collision rates that heats the gas.[8] Nevertheless, in this work, the power is fixed at 200 W, and the ionizing degree, 0.1%, is accordingly far lower than the above threshold, in a chamber with more or less the same size. Hence, it is believed that the findings of this model that aims at revealing gas flow characteristics ought to be insignificantly influenced if excluding the gas heating effect. In addition, the gas temperature increases with pressure due to high feedstock molecule density that increases the collision rates,[12] and hardly changed with flow rate, as observed in the experiment of Ref. [43]. These new features of gas heating effect, on the other hand, authenticate this discovery on the gas flow effect that is carried out at low pressure, 20 mTorr. As noted, the present study successfully decouples the gas flow and heating effects. This is useful for us to see each role of the effects in the discharge dynamics.

As we understood, the ion temperature is important in addressing the spatial transport of charged species via the diffusion and mobility of ions, and correlated to the gas heating effect via the elastic and charge exchange collisions between the charged and neutral species, which transfer energy from ions to neutrals. One paper has reported that the axial and radial profiles of plasma density, temperature and potential agreed well with the experiment, based on the ion mobility data predicted by the Monte Carlo technique and the local field approximation that calculates ion temperature, which is used to calculate the diffusion via the Einstein's relation.[44] We believe that properly addressing ion temperature can be very helpful for the model to predict well the spatial characteristics of charged species. Clearly, this is out of the scope of the present work, which is focused on the gas flow effect. On the other hand, as found in our work, the ion density profile is not changed by the gas flow, due to the fact that the ion directional velocity is always several orders higher than the gas flow velocity. Therefore, we believe that the present work that attempts to reveal the qualitative trends of plasma against the gas flow, be insignificantly affected by utilizing room temperature assumption for the ions. Still, as the gas heating effect is less important at this low power selected in this work, the influence of ion temperature on the gas temperature[5] is therefore of no interest.

In the present work, the steady state gas flow equation is used. This indicates that plasma was produced and transported on one already established fields of flow velocity and mixture density. Hence, the influence of gas flow on the plasma is well explained. Nevertheless, the influence of plasma generation and transport on the gas flow is not properly addressed. Still, this is a two-dimensional simulation, hence the gas flow behavior across the radial and axial plane cannot be described yet. To sum up, in future works, it is expected that more insights about the gas dynamics can be revealed by considering the gas temperature and ion temperature kinetics, and meanwhile introducing the unsteady state and full dimensional gas flow equation.

## Appendix A

Usually, the inductive discharges can operate on two modes, *i.e.*, E and H modes. The mode transition is a very interesting topic that attracts much attentions.[45–48] As we mentioned in Subsubsection 2.2.3, the electromagnetic equation we gave, *i.e.*, Eq. (11), can describe both the two discharge modes. Nevertheless, our gas flow study is conducted in the H mode. In the appendix, we plan to show explicitly how to use that vector electromagnetic equation to describe the H mode discharge.

First, we deduce Eq. (11) from the Maxwell's equations, via the magnetic vector potential. The full Maxwell equation set is described as

$$\begin{aligned}
&\nabla \times \boldsymbol{H} = \boldsymbol{J} + \frac{\partial \boldsymbol{D}}{\partial t},\\
&\nabla \times \boldsymbol{E} = -\frac{\partial \boldsymbol{B}}{\partial t},\\
&\nabla \cdot \boldsymbol{B} = 0,\\
&\nabla \cdot \boldsymbol{D} = \rho.
\end{aligned}$$

In the above equations, considering that the magnetic field is passive and rotational field, we can introduce the magnetic vector potential to describe the magnetic field, $\boldsymbol{B} = \nabla \times \boldsymbol{A}$. Besides, in the ICP simulations, the usual way of solving the electric field is dividing it into two parts, *i.e.*, electromagnetic-induced and electrostatic fields. The Poisson's equation is used to describe the electrostatic field, and the Maxwell equations are used to describe the electromagnetic-induced field. Hence, in the above Maxwell equations, the electric charge density is set as $\rho = 0$, and accordingly, the electric field component that is induced by the electromagnetic effect in the Maxwell's equations is a passive and rotational field, which can be expressed as $\boldsymbol{E} = -\partial \boldsymbol{A}/(\partial t)$. The conductive current

density includes two parts, *i.e.*, $\boldsymbol{J} = \boldsymbol{J}_{\rm a} + \boldsymbol{J}_{\rm p}$, where $\boldsymbol{J}_{\rm a}$ is the applied coil current density and $\boldsymbol{J}_{\rm p} = \sigma \boldsymbol{E}$ is the plasma current density. By further using the harmonic wave approximation, we can deduce the equation of Eq. (11), *i.e.*,

$$\left(\mathrm{j}\omega\sigma - \omega^2\varepsilon_0\varepsilon_{\rm r}\right)\boldsymbol{A} + \nabla \times \nabla \times \left(\mu_0^{-1}\mu_{\rm r}^{-1}\boldsymbol{A}\right) = \boldsymbol{J}_{\rm a}.$$

We now observe the H mode discharge by means of this equation. We know that the in the H mode, the radial and axial components of magnetic field and the azimuthal component of electric field work. Hence, we only need to consider the azimuthal component of the above vector equation, namely,

$$\left(\mathrm{j}\omega\sigma - \omega^2\varepsilon_0\varepsilon_{\rm r}\right)A_\theta + \nabla^2\left(\mu_0^{-1}\mu_{\rm r}^{-1}A_\theta\right) = J_{{\rm a},\theta}.$$

This is the scalar equation that describe the H mode discharge of ICP. After $A_\theta$ is calculated, the azimuthal electric field can be calculated as, $E_\theta = -\partial A_\theta/(\partial t) = -\mathrm{j}\omega A_\theta$.

## References


[1] Jayapalan K K and Chin O H 2015 *AIP Conf. Proc.* **1657** 150003
[2] Li H, Xiao C, Zhang E, Singh A K and Hirose A 2011 *Radiat. Eff. Defects Solids* **166** 399
[3] Han D M, Liu Z G, Liu Y X, Zhang X P, Gao F, Peng W and Wang Y N 2016 *J. Appl. Phys.* **119** 113302
[4] Agarwal A, Rauf S and Collins K 2012 *Plasma Sources Sci. Technol.* **21** 055012
[5] Hebner G A 1996 *J. Appl. Phys.* **80** 2624
[6] Kiehlbauch M W and Graves D B 2001 *J. Appl. Phys.* **89** 2047
[7] Hash D B, Bose D, Rao M V V S, Cruden B A, Meyyappan M and Sharma S P 2001 *J. Appl. Phys.* **90** 2148
[8] Lee H C, Seo B H, Kwon D C, Kim J H, Seong D J, Oh S J, Chung C W, You K H and Shin C 2017 *Appl. Phys. Lett.* **110** 014106
[9] Jayapalan K K and Chin O H 2014 *Phys. Plasmas* **21** 043510
[10] Shimada M, Tynan G R and Cattolica R 2008 *J. Appl. Phys.* **103** 033304
[11] Shimada M, Tynan G R and Cattolica R 2007 *Plasma Sources Sci. Technol.* **16** 193
[12] O'Connell D, Gans T, Crintea D L, Czarnetzki U and Sadeghi N 2008 *J. Phys. D: Appl. Phys.* **41** 035208
[13] Takahashi K, Chiba A, Komuro A and Ando A 2015 *Phys. Rev. Lett.* **114** 195001
[14] Fruchtman A and Makrinich G 2005 *Phys. Rev. Lett.* **95** 115002
[15] Kobayashi J, Nakazato N and Hiratsuka K 1989 *J. Electrochem. Soc.* **136** 1781
[16] Park S K and Economou D J 1990 *J. Electrochem. Soc.* **137** 2624
[17] Sekine M 2002 *Pure Appl. Chem.* **74** 381
[18] Lymberopoulos D P and Economou D J 1995 *IEEE Trans. Plasma Sci.* **23** 573
[19] Chinzei Y, Ichiki T, Ikegami N, Feurprier Y, Shindo H and Horiike Y 1998 *J. Vac. Sci. Technol. B* **16** 1043
[20] Kim H J, Yang W and Joo J 2015 *J. Appl. Phys.* **118** 043304
[21] Okhrimovskkyy A, Bogaerts A and Gijbels R 2004 *J. Appl. Phys.* **96** 3070
[22] Tong L Z 2012 *Cent. Eur. J. Phys.* **10** 888
[23] Xu X, Feng J, Liu X M, Wang Y N and Yan J 2013 *Vacuum* **92** 1
[24] Doh H H and Horiike Y 2001 *Jpn. J. Appl. Phys.* **40** 3416
[25] Tong L Z 2013 *Jpn. J. Appl. Phys.* **52** 05EA03
[26] Tinck S, Tillocher T, Dussart R, Neyts E C and Bogaerts A 2016 *J. Phys. D: Appl. Phys.* **49** 385201
[27] Kim H J and Lee H J 2016 *Plasma Sources Sci. Technol.* **25** 035006
[28] Kiehlbauch M W and Graves D B 2003 *J. Vac. Sci. Technol. A* **21** 116
[29] Ventzek Peter L G, Grapperhaus M and Kushner M J 1994 *J. Vac. Sci. Technol. B* **12** 3118
[30] Panagopoulos T, Kim D, Midha V and Economou D J 2002 *J. Appl. Phys.* **91** 2687
[31] Lymberopoulos D P and Economou D J 1995 *J. Res. Natl. Inst. Stand. Technol.* **100** 473
[32] Li H, Liu Y, Zhang Y R, Gao F and Wang Y N 2017 *J. Appl. Phys.* **121** 233302
[33] Lee H C and Chung C W 2012 *Phys. Plasmas* **19** 033514
[34] Lee H C, Lee M H and Chung C W 2010 *Appl. Phys. Lett.* **96** 041503
[35] Chung C W and Chung H Y 2000 *Phys. Plasmas* **7** 3826
[36] Brezmes A O and Breitkopf C 2015 *Vacuum* **116** 65
[37] COMSOL 4.2 Userbook.
[38] Bird R B, Stewart W E and Lightfoot E N 2007 *Transport phenomena*, 2nd edn. (New York: John Wiley & Sons)
[39] Thompson P A 1998 *Compressible Fluid Dynamics* (New York: McGraw-Hill)
[40] Gao F, Zhao S X, Li X S and Wang Y N 2009 *Phys. Plasmas* **16** 113502
[41] Keesee A M and Scime E E 2006 *Rev. Sci. Instrum.* **77** 4091
[42] Zhao S X, Zhang Y R, Gao F, Wang Y N and Bogaerts A 2015 *J. Appl. Phys.* **117** 243303
[43] Abada H, Chabert P, Booth J P, Robiche J and Cartry G 2002 *J. Appl. Phys.* **92** 4223
[44] Mouchtouris S and Kokkoris G 2016 *Plasma Sources Sci. Technol.* **25** 025007
[45] Zhang X, Yu P C, Liu Y, Zheng Z, Xu L, Wang P and Cao J X 2015 *Phys. Plasmas* **22** 103509
[46] Zhang X, Cao J X, Liu Y, Wang Y P, Yu P C and Zhang Z K 2017 *IEEE Trans. Plasma Sci.* **45** 338
[47] Zhang X, Zhang Z K, Cao J X, Liu Y and Yu P C 2018 *AIP Adv.* **8** 035121
[48] Zhang Z K, Zhang X, Cao J X, Liu Y, Wang P and Yu P C 2018 *IEEE Trans. Plasma Sci.* **46** 3151